Brain Structure and Function (2019) 224:1489–1503
https://doi.org/10.1007/s00429-019-01850-8

ORIGINAL ARTICLE

Phase fMRI informs whole-brain function connectivity balance across lifespan with connection-specific aging effects during the resting state

Zikuan Chen[1] · Qing Zhou[2] · Vince Calhoun[1,3]

Received: 28 September 2018 / Accepted: 19 February 2019 / Published online: 2 March 2019

Abstract

A functional magnetic resonance imaging (fMRI) experiment produces complex-valued images consisting of pairwise magnitude and phase images. As different perspective on the same magnetic source, fMRI magnitude and phase data are complementary for brain function analysis. We collected 600-subject fMRI data during rest, decomposed via group-level independent component analysis (ICA) (mICA and pICA for magnitude and phase respectively), and calculated brain functional network connectivity matrices (*mFC* and *pFC*). The *pFC* matrix shows a fewer of significant connections balanced across positive and negative relationships. In comparison, the *mFC* matrix contains a positively-biased pattern with more significant connections. Our experiment data analyses also show that human brain maintains a whole-brain connection balance in resting state across an age span from 10 to 76 years, however, phase and magnitude data analyses reveal different connection-specific age effects on significant positive and negative subnetwork couplings.

Keywords BOLD fMRI · Independent component analysis (ICA) · Functional network connectivity (FC) · Resting state · Functional connectivity balance · Age effect

Abbreviations

BOLD	Blood oxygenation level dependent
fMRI	Functional magnetic resonance imaging
FDR	False discovery rate
mICA	Magnitude-data independent component analysis (ICA)
pICA	Phase-data ICA
mFC	Magnitude-depicted function network connectivity (FC)
pFC	Phase-depicted FC

✉ Zikuan Chen
zchen@mrn.org

[1] The Mind Research Network and LBERI, 1101 Yale Blvd NE, Albuquerque, NM 87106, USA

[2] School of Physics and Astronomy, Yunnan University, Kunming 650091, China

[3] Department of Electrical and Computer Engineering, University of New Mexico, Albuquerque, NM 87131, USA

Introduction

The non-invasive blood oxygenation level-dependent (BOLD) functional magnetic resonance imaging (fMRI) method has been widely accepted for neuroimaging and brain function study. In MRI principle, a BOLD fMRI experiment produces a time series of complex-valued images from sinusoidal signals, consisting of pairwise magnitude and phase components. Of these, the magnitude has been traditionally considered as the default MRI output, and phase data is typically discarded. Since both magnitude and phase signals are different views of the same magnetic source (internal magnetic field distribution) (Chen and Calhoun 2011, 2013), they both have the potential to be useful for the study of brain function.

The rationale for using fMRI phase data for brain function study can be motivated by MRI physics (Chen and Calhoun 2013, 2015; Kee et al. 2017; Rowe 2005; Schweser et al. 2016). An fMRI phase image (unwrapped) is considered a representation of internal magnetic field map. Due to a dipole effect, this map is different from the underlying brain tissue magnetic susceptibility source. However, phase fMRI can be linearly approximated in the small phase angle regime image (Chen and Calhoun 2013), especially

for small relative temporal phase changes associated with a brain BOLD response (Chen and Calhoun 2015; Chen et al. 2018b). In past years, there has been a body of reports on the exploration and use of phase fMRI (or its inference) for brain function study (Arja et al. 2009; Balla et al. 2014; Bianciardi et al. 2014; Chen and Calhoun 2016; Feng et al. 2009; Ozbay et al. 2016; Rowe 2005, 2009). We have recently reported on utilizing both magnitude and phase data to study brain functional connectivity in the resting state (Chen et al. 2018a). In this report, we extend our previous study with a much larger ($N=600$) analysis and focus on new aspects of resting functional connectivity and its relationship with age.

Given an fMRI timeseries, we can decode the data into a collection of intrinsic functional networks using independent component analysis (ICA) (Aragri et al. 2006; Li et al. 2007; McKeown et al. 2003; McKeown and Sejnowski 1998). Taking advantage of data-driven multivariate statistics, ICA has been successfully developed for group-level data analysis (a group ICA) (Abou Elseoud et al. 2011; Calhoun et al. 2001, 2009; Du et al. 2015; Guo and Pagnoni 2008; Xu et al. 2013), applicable for both resting-state and task-related function analyses. The ICA method has also been applied to fMRI magnitude and phase data analyses separately, denoted by mICA and pICA(Chen et al. 2018a). To compare pICA with mICA more directly, we can constrain pICA with the mICA-inferred group information, thus implementing a group-information-guided (GIG) pICA (Du and Fan 2013). Therein, we calculated their functional network connectivity (FC) matrices, denoted by *mFC* and *pFC*, respectively, based on the temporal correlation of mICA and GIG-pICA timecourses (Arbabshirani and Calhoun 2011; Jafri et al. 2008).

An FC matrix consists of positive and negative connections, in which a large positive value represents a high-correlation connection (or coupling) between specific subfunctions, whereas a negative value represents an anticorrelation. The correlation and anticorrelation cancellation creates a balance in the low-frequency network connections (Chen et al. 2018a; Fox et al. 2005, 2009; Litwin-Kumar and Doiron 2012; Marino et al. 2005; Murphy et al. 2009), which can be quantified via the FC matrix mean, denoted by mean(*mFC*) (Chen et al. 2018a). A small |mean(*mFC*)| value (close to 0) implies a balance of whole-brain connectivity. Recently, a balanced network has been observed based on magnitude data analysis in high-frequency microcircuits (Litwin-Kumar and Doiron 2012; Liu et al. 2015; Marino et al. 2005). It has been reported (Lewis et al. 2016) that fast fMRI can detect oscillatory neural activity in humans. With the advent of spatiotemporal fMRI, network balance has been measured at low-frequency subnetworks (a timescale of minutes) (Adhikari et al. 2017; Caliandro et al. 2017; Kringelbach et al. 2011). Through our 600-subject experiment we show in this report that the fMRI phase data analysis shows more balance in resting-brain function connectivity, as denoted by $|\text{mean}(pFC)| < |\text{mean}(mFC)|$.

We are also concerned with the longitudinal evolution of the resting-brain functional connectivity with respect to age. Our results from the 600-subject data analysis include the following: (1) the phase data show that the positive couplings in resting-brain FC are slightly increased in older individuals, whereas the negative couplings are slightly decreased; in comparison, the magnitude data show an opposite age-correlation behavior. (2) Whole-brain FC (either magnitude or phase) maintains a balance over the age span due to the cancellation of positives and negatives in the FC matrix. Intuitively, it seems reasonable to observe a normal human brain that maintains a balanced functional connectivity in resting state from a young (10 years) to old (76 years) age. The fMRI magnitude and phase data analyses show distinct brain function connectivity behavior as the brain grows in age. We advocate for the inclusion of complementary information from the fMRI phase data in studies of functional connectivity.

Materials and methods

Data collection and processing

A collection of 600 subject datasets (different in subject) were acquired from a cohort of healthy participants (346 male, age 10–76) by scanning subjects (in a few days) in a Siemens TrioTim 3 T scanner at the Mind Research Network. Informed consent was obtained for each subject and the subject scanning protocol was approved by the IRB at the University of New Mexico. The data were anonymized prior to group analysis. Brain imaging was performed with the following parameter settings: 12-channel coil, GRE-EPI sequence, TE = 29 ms, TR = 2 s, flip angle = 75°, field of view = 240 cm × 240 cm, matrix size = 64 × 64, voxel size = 3.75 mm × 3.75 mm × 4.55 mm, slice thickness = 3.5 mm, slice gap = 1.05 mm, acquisition time (TA) = 5 min, total volumes 152. Subjects were instructed to keep their eyes open during the scanning and fixate on the foveally presented cross.

The fMRI magnitude images were preprocessed based SPM8 (http://www.fil.ion.ucl.ac.uk/spm/software/spm8/) using an automated pipeline as reported in (Allen et al. 2014; Chen et al. 2018a). Preprocessing included the removal of the first 4 timepoints to avoid T1 equilibration effects, realignment using INRIalign, slice-timing correction using the middle slice as the reference frame, spatial normalization into MNI space with resampled isotropic voxels (3 mm × 3 mm × 3 mm), and spatial smoothing with a Gaussian kernel (with a full width as half maximum FWHM = 9 mm). Both brain magnitude and phase data

were spatially masked (using a spatial binary mask generated from magnitude image analysis) so as to confine the region-of-interest inside the intracranial region (excluding head scalp and brain cavity).

Extracting BOLD-only phase signals

The raw phase images were first converted to a range in $[-\pi, \pi]$ rad, denoted by $P[\mathbf{r}, t]$. Then, the phase series images were subjected to the spatial realignment through the 3D affine transformation using the motion correction parameters (in a 4×4 affine transformation) as derived from the magnitude image realignment in the corresponding magnitude time series (Chen et al. 2018a). Upon the phase time series image realignment, a complex-division was used to extract the temporal phase changes (BOLD-only phase response) with respect to the middle frame (at the middle timepoint in the series) (Chen and Calhoun 2016; Chen et al. 2018b), denoted by $\delta P[\mathbf{r}, t]$. To a great extent, the complex division serves a time-domain phase-unwrapping technique, which can extract the small temporal phase changes ($\ll \pi$) buried in the phase-wrapped time series signals (Chen and Calhoun 2015, 2016). Note that the number of timepoints in $\delta P[\mathbf{r}, t]$ is 1 less than that in $P[\mathbf{r}, t]$. Finally the $\delta P[\mathbf{r}, t]$ time series were subject to spatial normalization and spatial smoothing as done for the magnitude time series. Both the preprocessed magnitude and phase time series were truncated at a number of 148 timepoints (the leading 4 timepoints were omitted).

Group mICA and GIG-pICA

The SPM-processed magnitude data were decomposed into functional networks using a group-level spatial ICA (Chen et al. 2018a) and implemented in the GIFT toolbox (http://mialab.mrn.org/software/gift/). We decomposed the magnitude data (a group of 600 subject datasets) into a number of 100 brain subfunctions (a relatively high model order brain functional ICA), denoted by mICA. In implementation, we stacked the 600 subject magnitude datasets into 2D group space×time matrix (600×148 in size) and performed infomax spatial ICA decompositions in 10 repetitions using ICASSO method (http://www.cis.hut.fi/projects/ica/icasso) to obtain a set of 100 aggregate spatiotemporal components, denoted by $\text{mICA}_n(\mathbf{r}, t)$ for $n = 1, 2, \ldots, 100$. Then we estimated subject-specific spatial maps ($\text{ICA}^j(\mathbf{r})$) and timecourses ($\text{ICA}^j(t)$), for $j = 1, 2, \ldots, 600$ using the GICA1 back-reconstruction method (Calhoun et al. 2001; Erhardt et al. 2011). From these, we selected a subset of 50 components (intrinsic connectivity networks) by excluding the ICAs that were obviously affected by physiological, motion, and imaging artifacts as characterized by non-cortical activation in spatial maps and high-frequency fluctuations in timecourses (see Allen et al. 2011, 2014; Beckmann et al. 2005 for selection details).

The timecourses mICA(t) were post-processed by (1) detrending linear, quadratic, and cubic trends, (2) removing outliers (with a replacement of local spline fit over the timecourse), and (3) low-pass filtering with a high-frequency cutoff of 0.15 Hz. Finally, the post-processed mICA(t) were normalized to have a unit variance such that the covariance matrices correspond to correlation matrices (Allen et al. 2014).

Considering the mICA maps as brain subfunction templates, we used them as group information to guide the group ICA decomposition of phase data $\delta P[\mathbf{r}, t]$, as implemented by a technique of GIG-ICA method (Du and Fan 2013). The GIG-pICA timecourses were then post-processed in similar ways as done for the mICA timecourse post-processing. It is noted that we conducted magnitude-guided GIG-pICA, rather than the independent pICA, to obtain the same order for maximal spatially-matched mICA and pICA maps. This facilitated the correspondence and comparison of mICA and pICA maps and their functional connectivity matrices (see below).

Arrangement of mICA and pICA components

In order to observe the pattern in an *mFC* matrix calculated from a collection of mICA timecourses, we need to arrange the mICA timecourses in a fixed order. According to brain structural and functional organization, we classified the 50 selected mICA components roughly into seven brain domains based on spatial activation locations (Allen et al. 2014), in an order of subcortical region (SC), auditory (AUD), sensorimotor (SM), visual (VIS), cognitive control (CC), default mode network (DMN), and cerebellum (CB). The number of intra-domain mICA networks may vary from domain to domain, depending on the number of mICA (initially specified for ICA decomposition and subsequently selected for brain subfunction representation). Within each domain, a small number of mICA components were ordered through a local clustering algorithm (Bullmore and Sporns 2009; Dodel et al. 2002; Rubinov and Sporns 2010) so as to reveal the within-domain functional parcellation (manifested in the consolidated on-diagonal blocks). It is pointed out that the pICA components were ordered in correspondence with the mICA ordering as ensured by the GIG-pICA method.

Calculation of {*mFC, pFC, mFCage, pFCage*} matrices

Upon calculation of $\{\text{mICA}^j(t)\}$ and $\{\text{pICA}^j(t)\}$, we developed pairwise temporal correlation matrices for each subject

j, denoted by mFC^j and pFC^j. Then, we calculated the group-level magnitude and phase FC matrices by

$$mFNC^j(n,n') = \mathrm{corr}\left(mICA_n^j(t), mICA_{n'}^j(t)\right)$$
$$pFNC^j(n,n') = \mathrm{corr}\left(pICA_n^j(t), pICA_{n'}^j(t)\right)$$
$$\forall n,\ n' \in [1,50], j \in [1,600],$$

where corr denotes a correlation (Pearson correlation), $mICA_n^j(t)$ denotes the timecourse of the magnitude ICA number n for the subject j, and other timecourses are denoted in the same manner.

Upon the calculation of $\{mFC^j\}$ and $\{pFC^j\}$, we calculated the group-averaged FC matrices, as defined by $mFC = \sum_j (mFC^j)/600$ and $pFC = \sum_j (pFC^j)/600$. Meanwhile, we obtained the statistical significances, in terms of p values, for mFC and pFC calculations by one sample t test, denoted by P_{mFC} and P_{pFC} respectively. In the result, we obtained a group-averaged mFC and P_{mFC} matrices (in size of 50×50) from magnitude data, and pFC and P_{pFC} matrices from phase data. After false discovery rate (FDR) correction (Genovese et al. 2002), we used the FDR-corrected p value matrices, P_{mFC} and P_{pFC}, to represent the statistical significances for thresholding mFC and pFC matrices.

Using the subject age as a variable, we calculated the age-correlated matrices and their p values by

$$[mFCage(n,n'), P_{\mathrm{mAge}}(n,n')] = \mathrm{corr}\left(mFC^{\mathrm{age}}(n,n'), \mathrm{age}\right)$$
$$[pFCage(n,n'), P_{\mathrm{pAge}}(n,n')] = \mathrm{corr}\left(mFC^{\mathrm{age}}(n,n'), \mathrm{age}\right)$$
$$\forall age \in [10,76],\ n,n' \in [1,50],$$

where we take two outputs from the Matlab corr routine. The p value matrices, P_{mAge} and P_{pAge}, were FDR-corrected (Genovese et al. 2002) and used as the statistical significances of $mFCage$ and $pFCage$ calculations.

Characterization of group *mFC* and group *pFC* matrices

For pattern analysis of mFC and pFC matrices, we propose to observe the following characteristics (Chen et al. 2018a):

1. An on-diagonal block (with high correlation values) of FC matrix defines a functional clique within a brain domain.
2. An off-diagonal block with high positive correlation values (negative correlation values, respectively) defines a correlative coupling (anticorrelation coupling) between ICA components across different brain domains.
3. The positive and negative connection balance in an FC matrix is characterized by a small mean value |mean(FC)| (close to 0).
4. The average connection strength in an FC matrix is characterized by std(FC) (a nonnegative standard deviation of all entries in the FC matrix).

Subject variability and age effect on brain function connectivity

We can numerically characterize the subject variability of magnitude and phase-depicted brain function connectivity in terms of mean(mFC^j) and mean(pFC^j) (with respect to the subject index j), respectively. A small value of |mean(mFC^j)| or |mean(pFC^j)| indicates a good connectivity balance. Meanwhile, we can numerically characterize the connectivity strength in terms of std(mFC^j), for example, for the magnitude data of subject j.

By specifying the subjects with ages, we can observe the age effect on $\{mFC^j\}$ and $\{pFC^j\}$. By line fitting of the scattering data with respect to age, we estimate the linear trend of the age effect. That is, we can use the $pFCage$ matrix pattern for an overview of the age effect on brain function couplings (intra-domain or inter-domain). We can also observe the individual scattering and assemble trend for specific subfunction couplings with respect to the brain age.

Results

Brain function decomposition (mICA and pICA)

We decomposed the group magnitude datasets by group ICA (denoted by mICA) to produce a set of 100 spatiotemporal components (denoted by $\mathrm{mICA}_n(\mathbf{r}, t)$ for $n = 1, 2, \ldots, 100$, each consisting of a spatial map $\mathrm{mICA}_n(\mathbf{r})$ and a timecourse $\mathrm{mICA}_n(t)$ in companion). Based on the spatial anatomical locations, we classified the selected 50 ICA components into seven brain domains in the following order: 4 components in subcortical region (SC, 4), 2 in auditory (AUD, 2), 8 in sensorimotor (SM, 8), 10 in visual (VIS, 10), 14 in cognitive control (CC, 14), 9 in default mode network (DMN,9), and 3 in cerebellum (CB, 3). In this domain partition and component ordering, all cross correlations among the ICA components are presented in a fixed matrix pattern (50×50). Moreover, a GIG-pICA algorithm was used for phase data analysis, which facilitates the correspondence of the mICA and pICA components. In the results, we obtained a set of 50 pairs of magnitude- and phase-depicted brain subfunctions from the 600-subject

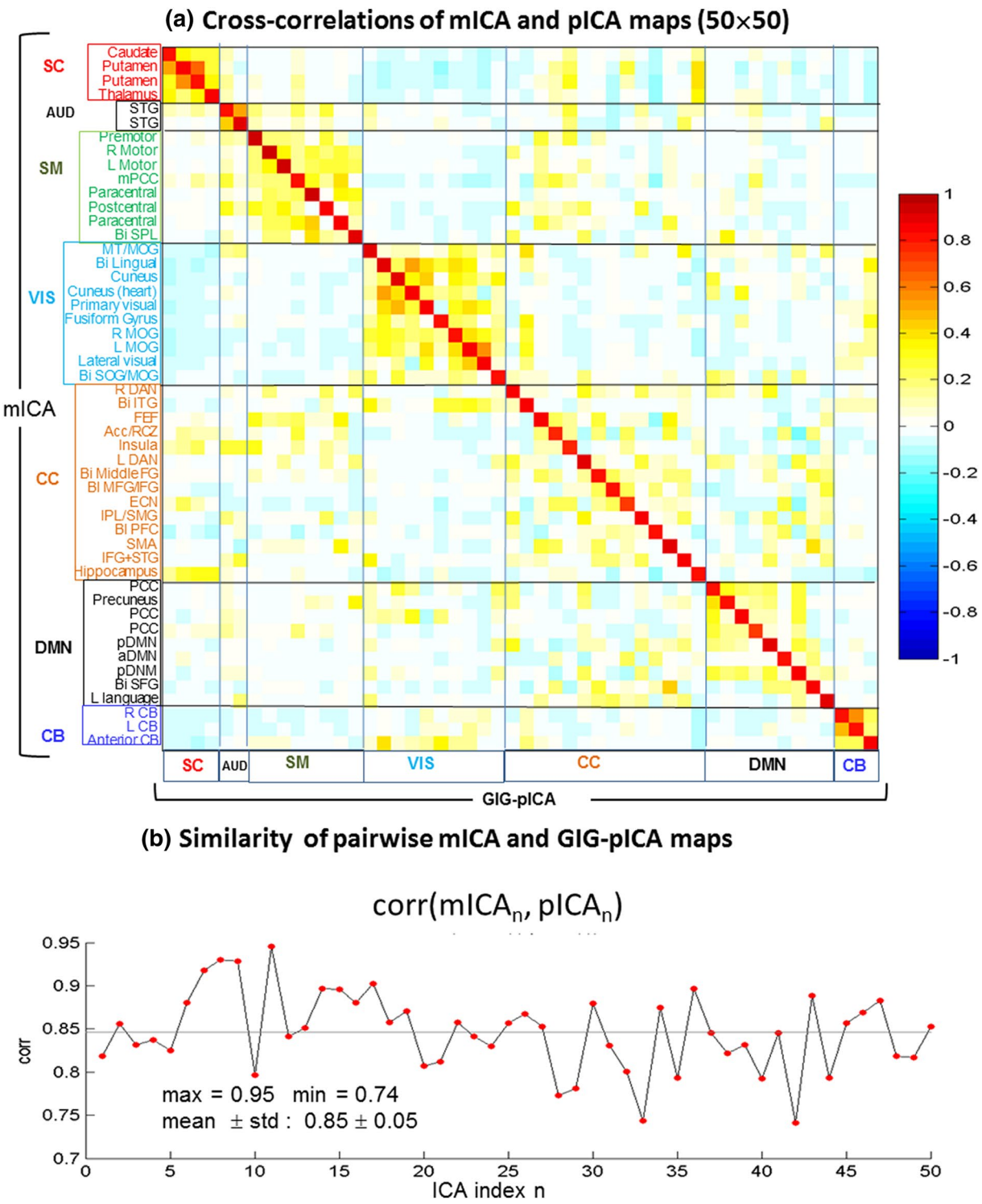

Fig. 1 Spatial correlations between mICA and pICA maps. **a** Spatial correlation matrix (*scorr* in size of 50×50) between 50 pairs of mICA and pICA maps, and **b** spatial correlations of the pairwise ($mICA_n(\mathbf{r})$, $pICA_n(\mathbf{r})$) maps, corresponding the values on the diagonal line of *scorr* matrix

magnitude and phase data. The spatial maps of the (mICA, pICA) pairs are displayed side-by-side in supplementary information Fig. S1.

In Fig. 1, we show the spatial correlation (*scorr*) matrix of mICA and pICA maps, defined by $scorr(n, n') = corr(mICA_n(\mathbf{r}), pICA_{n'}(\mathbf{r}))$ for $n, n' = 1, 2, \ldots, 50$. Note that the 50×50 *scorr* matrix takes on the

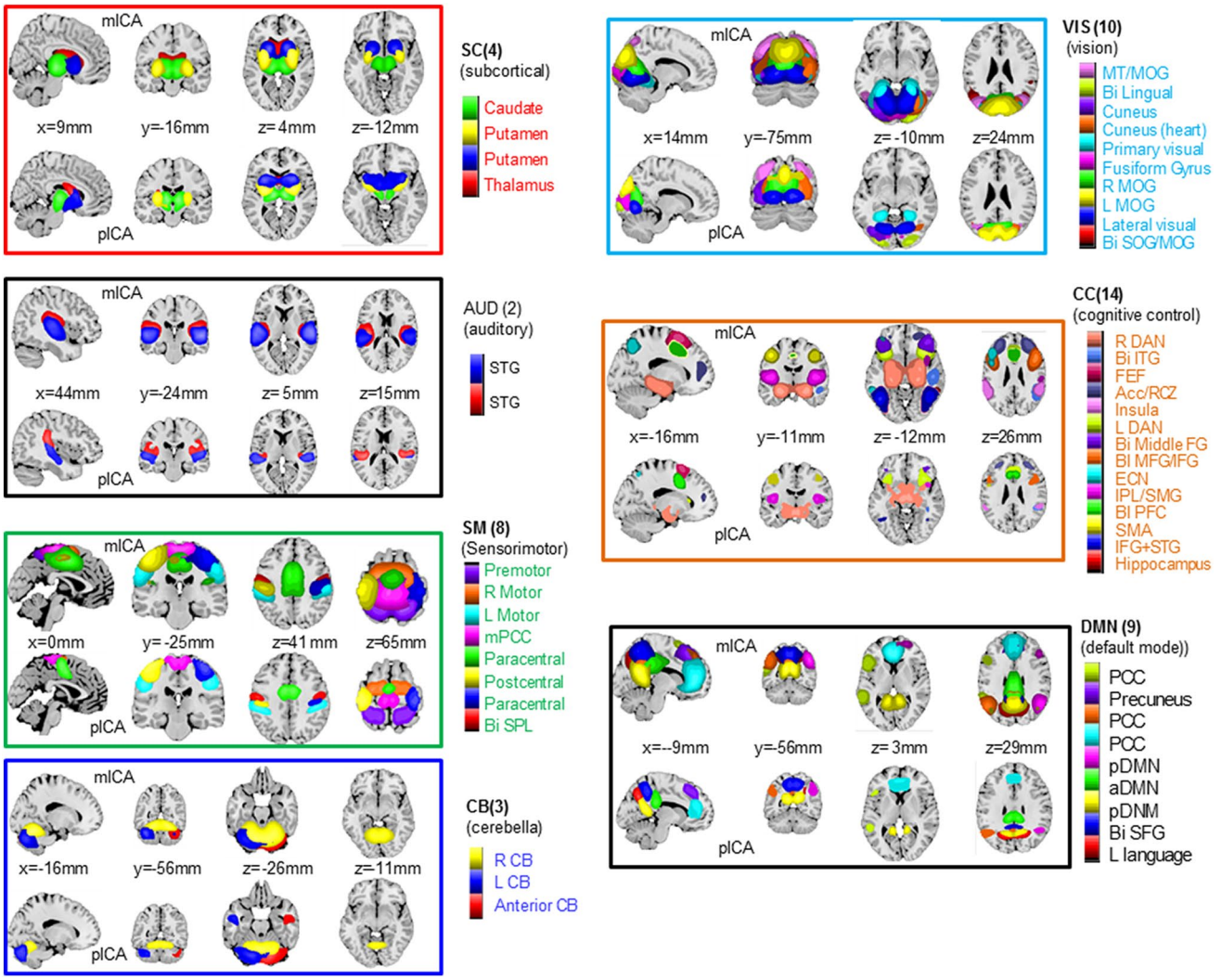

Fig. 2 Color-coded displays of the thresholded mICA and pICA maps. The 50 pairs of (mICA, pICA) maps were color-coded displays in seven boxes for seven brain domains (SC(4), AUD(2), SM(8), VIS(10), CC(14), DMN(9), CB(3)). Each spatial map (a 3D volume) was displayed with three orthogonal *x*-, *y*-, *z*-slices across the maximally-activated blob foci and one extra distant *z*-slice

aforementioned ICA component arrangement at the left side label. The diagonal line of the *scorr* matrix represents the spatial similarity of the pairs ($mICA_n$, $pICA_n$). More numerically, the on-diagonal line values are plotted in Fig. 1b, assuming correlations in a range [0.74, 0.95].

For visualization of the ICA-decomposed brain subfunctions, in Fig. 2 we show the color-coded spatial maps of the pairwise mICA and pICA activation patterns in each domain. Specifically, we display the mICA and pICA maps (3D volumes) using four slices: three orthogonal *x*-, *y*-, *z*-slices across major activation foci, and one extra *z*-slice at a distance to the major foci (in MNI coordinates).

Brain function connectivity (*mFC* and *pFC*)

We calculated subject-specific FC matrices, denoted by $\{mFC^j\}$ and $\{pFC^j\}$. By averaging over 600 subjects, we obtained the group-level FC matrices: *mFC* and *pFC* in size of 50×50, which are shown in Fig. 3a, b (the lower triangles of the symmetric matrices). Both *mFC* and *pFC* matrices consist of positive and negative correlations and are balanced to differing degrees in whole-brain functional connectivity. In terms of mean(*mFC*) and mean(*pFC*) for connectivity balance at macroscopic network level (Chen et al. 2018a), we note that the phase data reveals more connectivity balance (mean(*pFC*) = −0.002, close to 0) than the magnitude data (mean(*mFC*) = 0.04) as determined by |mean(*pFC*)| < |mean(*mFC*)|. The *mFC* and *pFC* matrices assume values of [−0.38, 0.74] and [−0.47, 0.83],

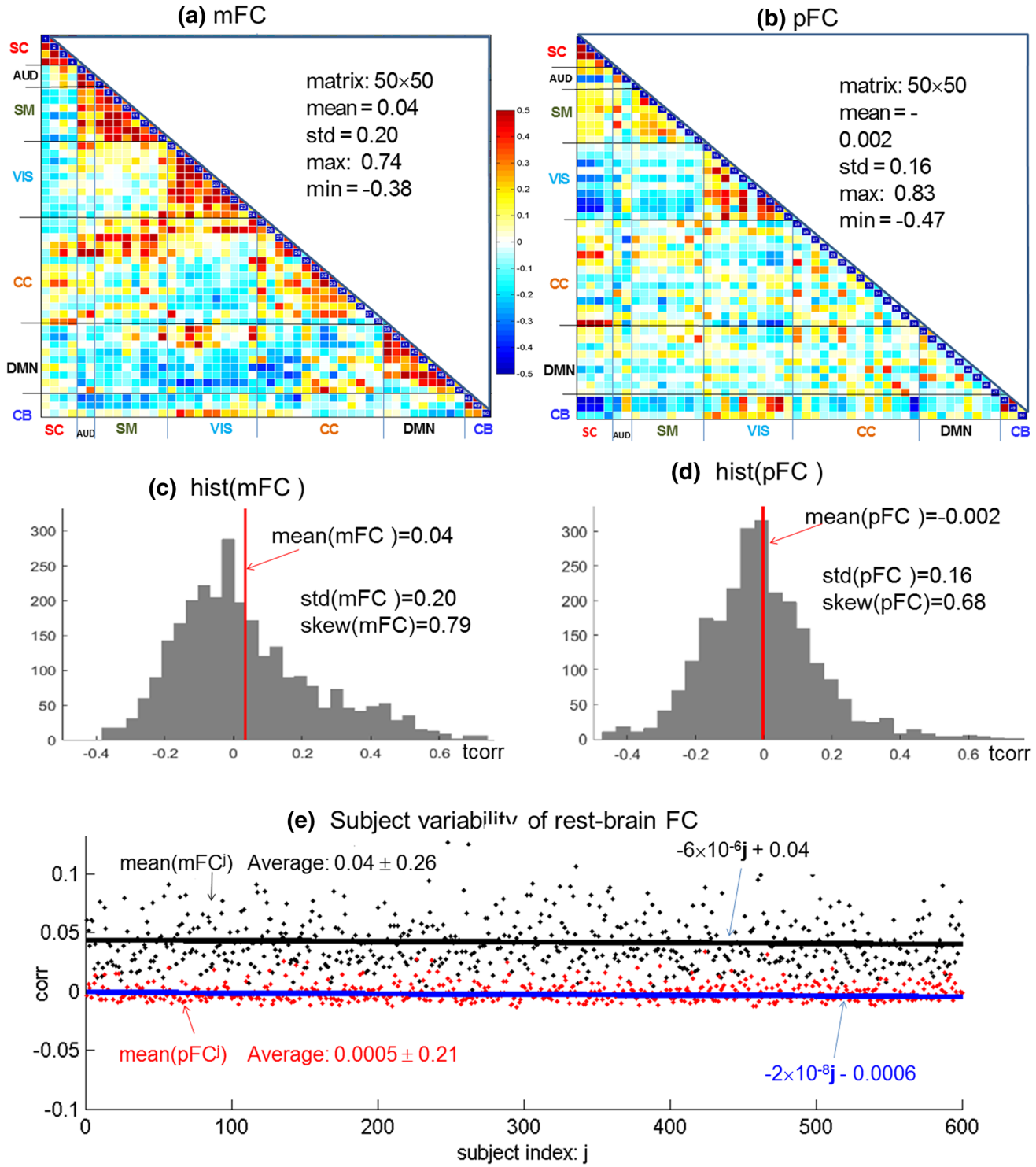

Fig. 3 Resting-state brain function network connectivity matrices (50×50) for magnitude and phase data. **a** The magnitude-depicted resting-brain function connectivity matrix (*mFC*) was calculated from 50 mICA timecourses; **b** the phase-depicted resting-brain function connectivity matrix (*pFC*) was calculated from 50 pICA timecourses in correspondence to the paired mICA; **c** the histogram of *mFC*; **d** the histogram of *pFC*; and **e** the matrix means of subject-specific connectivity matrices $\{mFC^j\}$ and $\{pFC^j\}$, for $j = 1, 2, \ldots, 600$

respectively. In Fig. 3c, d we show the histograms of *mFC* and *pFC* matrices together with the statistical values {mean, std, skew}. It is seen that the *pFC* histogram is more symmetrical than the *mFC* histogram (also determined by skew (*mFC*) = 0.79 > skew(*pFC*) = 0.68), which explains the more positive/negative cancellation in *pFC* than in *mFC*. Besides the group *mFC* and *pFC* analyses, we are also concerned with the individual subject-specific connectivity balance in $\{mFC^j\}$ and $\{pFC^j\}$ matrices. In Fig. 3c we show the scattering of mean(mFC^j) (in black dots) and mean(pFC^j) (in red dots) for 600 subjects, which show the subject variability of resting-state whole-brain connectivity. By line fitting, we observe that the whole-brain connectivity remains a rough connectivity balance across the 600 subjects (e.g. mean(mFC^j): $-6\times10^{-6}j+0.04$ and mean(pFC^j): $-2\times10^{-8}j-0.0006$).

Age-correlated FC matrices: *mFCage* and *pFCage*

By specifying subject age, denoting $\{mFC^j\}$ and $\{pFC^j\}$ by $\{mFC^{age}\}$ and $\{mFC^{age}\}$ for age ∈ [10, 76] years instead, we observed the age effect on individual brain FC balance as plotted in Fig. 4a. It is seen that there is no noticeable impact of age on individual whole-brain FC balance, as denoted from the flat fitting lines in very small |slope| (3e−4 for mFC^{age} fitting and − 3e−6 for pFC^{age} fitting). That is, the

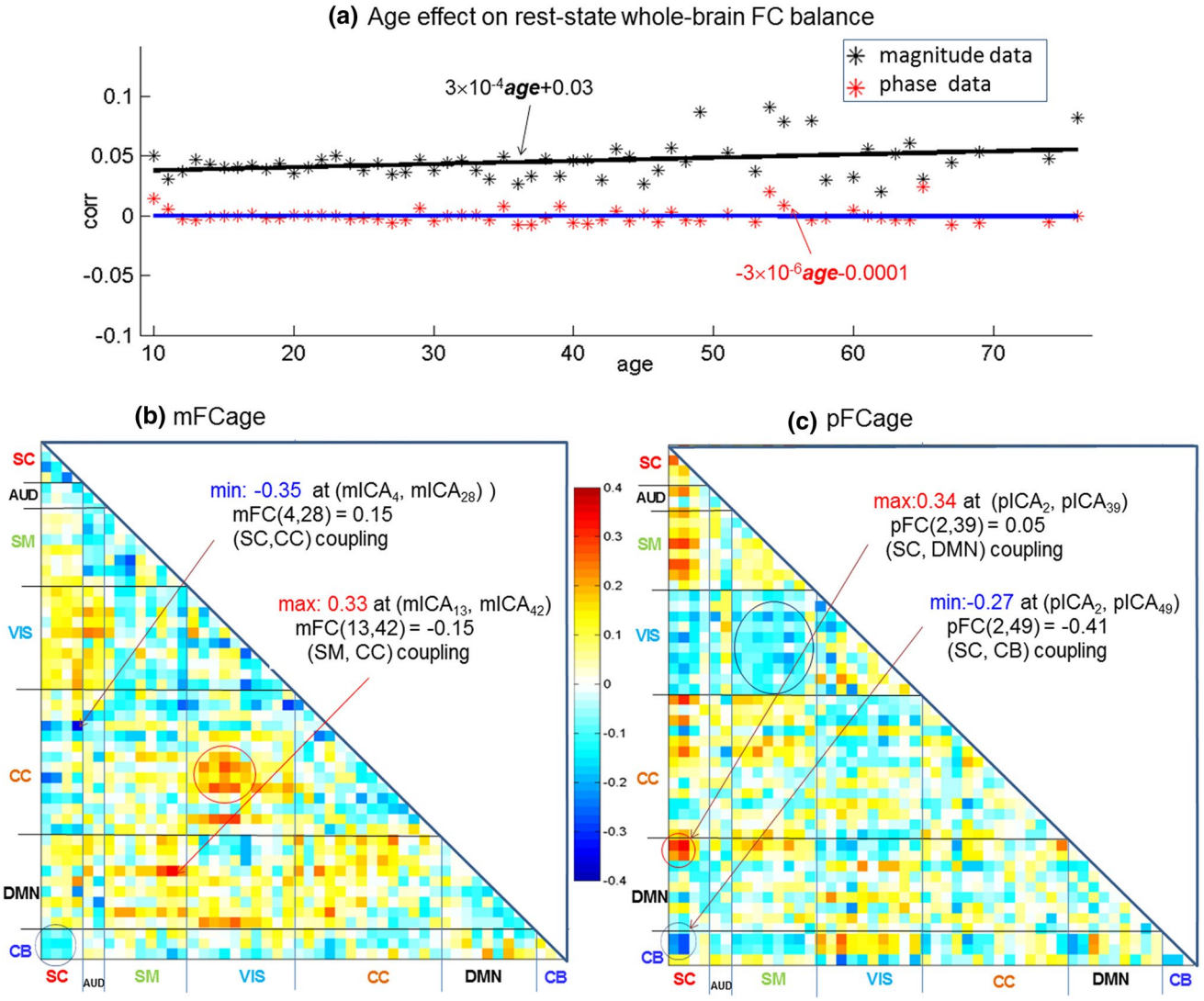

Fig. 4 Age effect on resting-brain full connectivity as depicted from magnitude and phase data. **a** Age effect on individual full brain connectivity balances in terms of mean(mFC^{age}) and mean(pFC^{age}) with an age span [10, 76] years for the 600-sbject experiment. **b** Age-correlated matrix *mFCage* (50×50 in symmetry) calculated by corr(mFC^{age}, age) for age = [10, 76]. **c** Age-correlated matrix *pFCage* (50×50) calculated by corr(pFC^{age}, age)

human brain connectivity balance (in terms of mean(mFC^j) and mean(pFC^j)) is consistent over the age span [10, 76] years. Next, we calculated two age-correlated FC matrices, denoted by *mFCage* and *pFCage* in size of 50×50, as shown in Fig. 4b, c.

In Fig. 4b, c, we notice that the max–min entries represent the extreme age-correlation values and the involved brain subfunctions may come from different brain domains. A large positive value in *mFCage* implies an ever-increasing coupling with age, and a negative value in *mFCage* implies a decreasing coupling with age. For example, in Fig. 4b, two subfunctions, $mICA_{13}$ from SM domain and $mICA_{42}$ from CC domain, which are negatively coupled with a correlation −0.14, and this coupling (SM, CC) increases with the subject's age by a maximal age correlation 0.33. That is, as the human brain grows in age, the negative coupling at ($mICA_{13}$, $mICA_{42}$) (a (SM, CC) coupling) increases with age by a correlation 0.33. In a similar manner, we may interpret the other entries in *mFCage* and *pFCage* matrices.

The points around the diagonal line in Fig. 4b are populated with dominant negative entries, representing anticorrelation between intra-domain coupling versus age. The magnitude data analysis shows that the intra-domain brain function couplings intend to decrease as the human brain grows in age. In comparison, in Fig. 4c we see different patterns from phase data analysis in the *pFCage* matrix. The positive and negative entries in the blocks (brain domains) along diagonal line are roughly cancelled, implying that the intra-domain couplings are positively and negatively correlated with age in a rough balance (connectivity balance in lifespan).

Age effect on significant couplings

The group-level *mFC* and *pFC* matrices were calculated from the assembly of 600 subjects, each was accompanied with a *p* value matrix representing statistical significance. We may use the *p* value matrix to select significant couplings for age effect observation. Specifically, we separated the

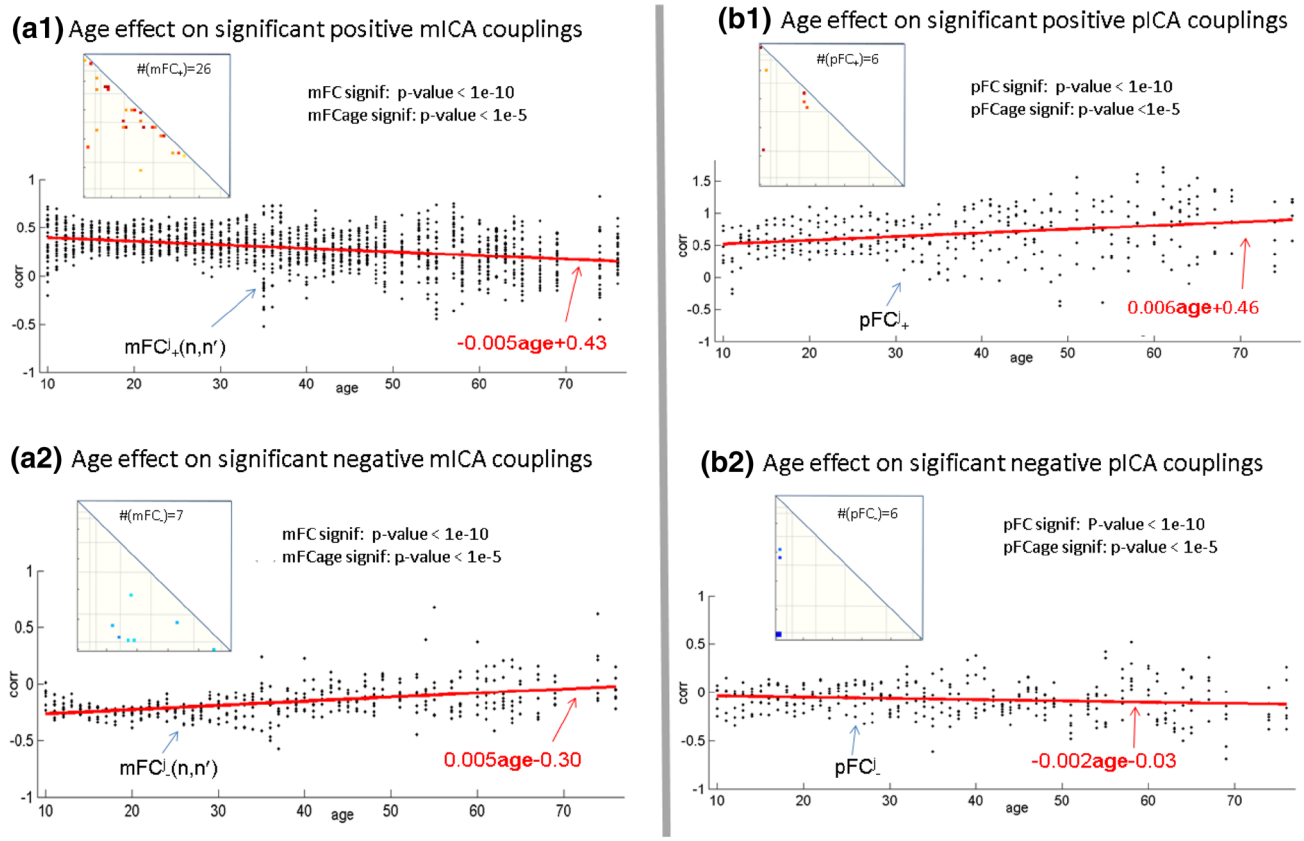

Fig. 5 Age effect on significant positive and negative brain subfunction couplings, **a1, a2** from magnitude data, and **b1, b2** from phase data. **a1** The significant positive couplings (in terms of mean(mFC^j_+)) evolve with respect to age. **a2** There are seven significant negative couplings from magnitude data (mean($mFC^j\_$) versus age). **b1** The significant positive couplings (in terms of mean(pFC^j_+)) evolve with respect to age. There are six significant positive couplings as determined by both the pFC significance (p value < 1e−10) and the *pFCage* significance (p value < 1e−5). **b2** There are six significant negative couplings from phase data (mean($pFC^j\_$) versus age)

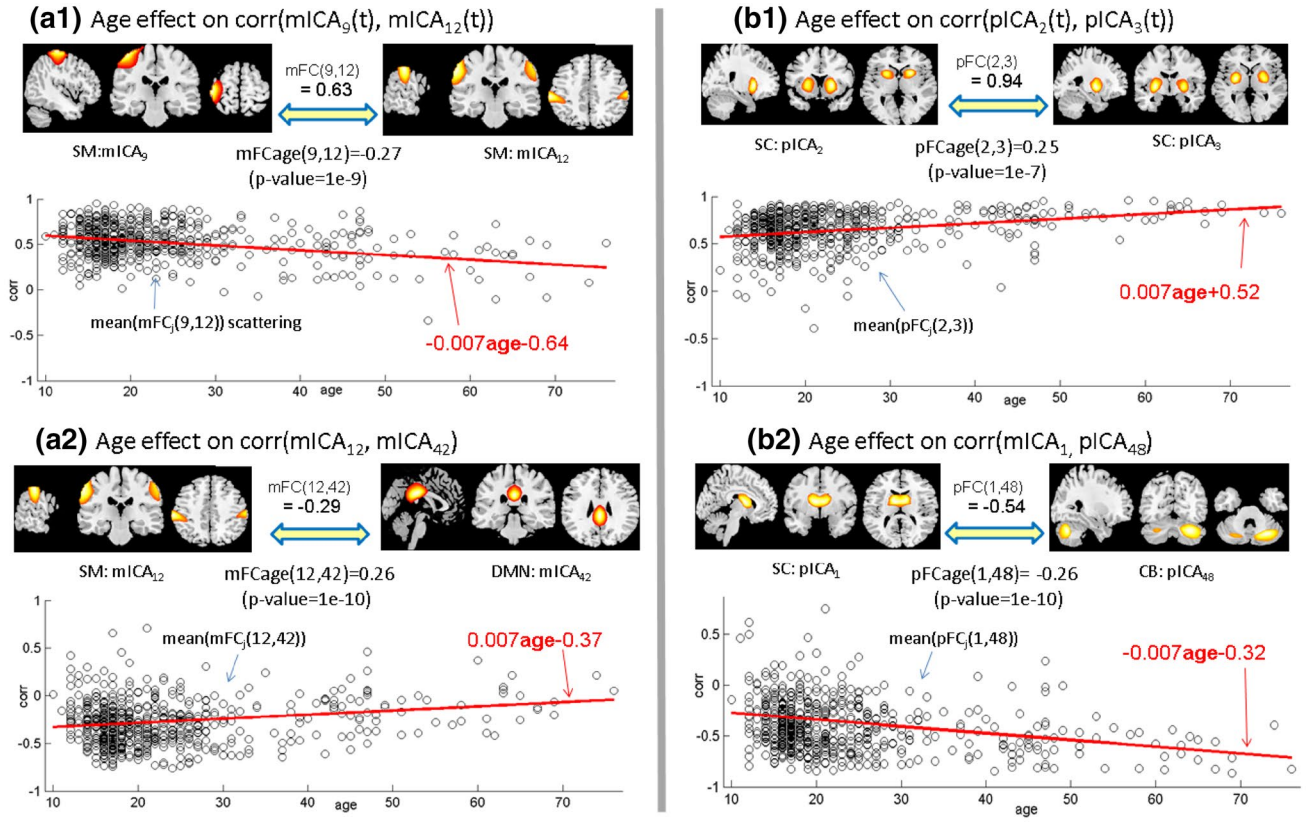

Fig. 6 Age effect on the most significant positive and negative brain subfunction couplings, **a1, a2** from magnitude data, and **b1, b2** from phase data. **a1** The most significant positive couplings at the coupling ($mICA_9$, $mICA_{12}$) as determined by both *mFC* and *mFCage*. **a2** The most significant negative couplings at the coupling ($mICA_{12}$, $mICA_{42}$). **b1** The most significant positive couplings at the coupling ($mICA_2$, $mICA_3$) as determined by both *pFC* and *pFCage* significances. **b2** The most significant negative couplings at the coupling ($pICA_1$, $pICA_{48}$). The involved subfunction maps are visualized in three orthogonal slices across the activation foci. The subfunction couplings are numerically characterized in $mFC(n, n')$ or $pFC(n, n')$ values

positive and negative entries and only look at the statistically significant entries (determined by p values). In Fig. 5a1, a2 we show that age effect on 26 significant positive couplings (denoted by mFC_+) and 7 significant negative couplings (denoted by $mFC\_$) as determined by both the *mFC* significance $p < 1e{-}10$ and the *mFCage* significance $p < 1e{-}5$. The line fitting over the scattered mFC_+ data produces a slowly decreasing line with a slope -0.005 with respect to age. Meanwhile, the line fitting over the scattered $mFC\_$ data produces a slowly increasing line with a slope 0.004. At the same statistical significance, we obtained 6 significant positive couplings (denoted by pFC_+) and 6 significant negative couplings (denoted by $pFC\_$), as shown in Fig. 5b1, b2. The line fittings over pFC_+ ($pFC\_$, respectively) produces a slowly increasing (decreasing) line with a slope of 0.006 (-0.002).

To further reduce the average effect, we are interested in the most significant couplings as found from each of the subsets $\{mFC_+, mFC\_, pFC_+, pFC\_\}$ at the maximal statistical significances. The results are shown in Fig. 6. Specifically, the magnitude data seen in Fig. 6a1 show that the most significant positive coupling happens at the coupling ($mICA_9$ vs $mICA_{12}$) within the SM domain. These are strongly coupled with a correlation 0.63 (group average), and this coupling decreases with age by a slope of -0.007 and a negative age correlation of -0.27. Conversely, we see in Fig. 6a2 the most significant negative coupling at ($mICA_{12}$ vs $mICA_{42}$) with a correlation -0.29, and this negative coupling increases with age by a slope of 0.007 and an age correlation of 0.26.

In comparison, we observed the age effect on most significant couplings in phase data in Fig. 6b1, b2. Specifically, we observed that the most significant positive coupling at ($pICA_2$vs $pICA_3$) (an intra-domain coupling within the SC domain) with a correlation 0.94, which increases with age by a slope of 0.007 and an age correlation of 0.25. Further, we observed the most significant negative coupling at ($pICA_1$ vs $pICA_{48}$) (an inter-domain coupling between SC and CB

domains) with a correlation −0.54, which decreases with the age by a slope of −0.007 and an age correlation of −0.26.

Discussion

Rationale of BOLD fMRI phase usage

The output of MRI is a complex-valued image (signal) in nature, consisting of pairing magnitude and phase. A BOLD fMRI experiment produces a time series of pairing magnitude and phase images simultaneously at no extra scan cost and, traditionally, only the magnitude signals are further analyzed. Since the phase signals are calculated from the same complex signals as used for the magnitude calculation (through a different transformation), the BOLD fMRI phase data are potentially useful for brain function analysis (Balla et al. 2014; Chen et al. 2018a; Ozbay et al. 2016). It is understood that a magnitude signal only takes nonnegative values, consequently and thus it cannot represent a bipolar-valued internal magnetic field distribution (e.g. $|\pm 1| = 1$) (2011, Chen and Calhoun 2013); whereas the phase calculation involves a trigonometrical function, arctan(x), which can be linearly approximated as $\arctan(x) \approx x$ for $|x| \ll 1$ rad (a small phase angle regime). Numerical simulations (Chen and Calhoun 2015) have shown that the arctan(x) nonlinearity is very weak such that phase fMRI can always be considered as a linear mapping in BOLD fMRI.

From a time series of fMRI phase images, we can extract the relative phase changes (δP) by a complex division algorithm. This technique enables us to extract the small BOLD-only phase responses ($|\delta P| \ll 1$ rad) from a time series of phase images (even for phase-wrapped images at timepoints). In reality, a BOLD-only phase response assumes a small phase angle regime [$|\delta P| \ll 0.2$ rad for 3T BOLD fMRI experiment (Chen et al. 2018a)] so as to alleviate phase nonlinearity. To an extent, in the sense of linear phase imaging, the fMRI phase data (δP images) are more suitable for brain interior depiction and brain function analysis.

Standard BOLD fMRI magnitude usage

BOLD fMRI has established the fMRI magnitude usage for standard brain function analysis. Indeed, a time series of raw BOLD fMRI magnitude images clearly show changes associated with dynamic brain states; in comparison, the raw phase images suffer from phase wrapping and heavy noise and the degree to which the phase is sensitive to in-flow or larger vessel effects is debated (Menon 2002). Therefore, the magnitude data are typically used for brain imaging. Since the (magnitude, phase) pairs are perfectly spatially coregistered, the magnitude-derived motion correction and spatial normalization parameters can also be applied to phase image processing (Chen et al. 2018a). In our report, we always compare brain function decomposition and functional network connectivity from magnitude and phase data simultaneously.

GIG-pICA for phase-based brain function decomposition

We used ICA for resting-state brain function decomposition. It is known that an ICA decomposition may produce different ICA components and a random output order from time to time due to the permutation ambiguity. In our group mICA decomposition, we specified a number of 100 components (a relative higher than the number of empirical brain subfunctions). Out of the 100 mICA components, we selected 50 components to represent the brain intrinsic networks (Allen et al. 2011, 2014). We then used the 50 selected mICA components to guide the phase data decomposition in a spatially constrained ICA algorithm called group-information-guided (GIG) pICA.

The GIG-pICA decomposition produces the same number of components in the same ordering as done from mICA, thereby facilitating the comparison of brain function analyses (mICA vs pICA) and the subsequent function connectivity correspondence (*mFC* vs *pFC*). We interpret our mICA and pICA decompositions as a collection of independent spontaneous activities (subfunctions) undergoing in human brain in a resting state.

Positive/negative connection balance in *mFC* and *pFC* matrices

An FC entry was calculated by the temporal correlation between two ICA-decomposed components, which may assume a positive or negative value. Intuitively, positive correlations are largely responsible for function integration whereas the negative correlations (anticorrelations) for function segregation, and both features are necessary for optimal information processing (Fox et al. 2005; Meadows 2011; Wu et al. 2011). The resting-state whole-brain function connectivity consists of both positive and negative correlations among independent spontaneous activities, either intra-domain or inter-domain couplings.

The positive/negative cancelation among the brain subfunction correlations can be numerically characterized in terms of the average of the whole FC matrix (Chen et al. 2018a). A balanced positive/negative correlation cancelation of FC leads to a small mean(FC) value (close to 0), implying the brain functional connection balance due to whole-brain correlation/anticorrelation cancelation. To our knowledge, only the magnitude data have been widely used for network balance study in low frequency regime (at timescale

of seconds) (Adhikari et al. 2017; Caliandro et al. 2017). The functional network balance has originally described by balanced excitation/inhibition mechanism in oscillatory activity at millisecond timescale (Litwin-Kumar and Doiron 2012; Liu et al. 2015; Marino et al. 2005). In this report, we explore phase-based resting-state whole-brain function connectivity at the timescale from seconds (TR = 2 s) to minutes (TA = 5 min) through a large group of fMRI phase data (from 600 subjects). Our experimental results (in Fig. 3) show that the phase data indicate better balance in brain function connectivity, as denoted by $|\text{mean}(pFC)| < |\text{mean}(mFC)|$, which are largely consistent with our previous 100-subject experiment (Chen et al. 2018a) despite of different phase data decomposition approaches.

Overall age effect on *mFC* and *pFC*

We observed an overall aging effect on resting-brain function connectivity in Fig. 4 as generated from both magnitude and phase data of 600 subjects (populated over an age span [10, 76] years). The results show that the resting-state human brain maintains a balance in whole-brain function connectivity at the macroscopic network level (in a time scale of seconds) as brain grows in age (linear trend $|\text{slope}| < 1e{-}4$). Concisely, both magnitude and phase data analyses show that the whole-brain connectivity of health human in resting state maintains a rough balance in the lifetime (Fig. 4a). Nevertheless, we also observed the distinct aging effects on the individual connections or subgroups in the *mFCage* and *pFCage* matrices (Fig. 4b, c).

Indeed, the diverse subfunctions imply the internal restlessness in an in vivo rest brain, and the aging effect consists of red (positive age correlation) and blue (negative age correlation) blocks (randomness in value and locations) in the *mFCage* and *pFCage* matrices in Fig. 4b, c. Specifically, through phase data analysis we can observe the positive aging effect with the following couplings in Fig. 4c: (1) the intra-SC couplings, (2) the (SC, VIS) couplings, and (3) part of the (SC, DMN) couplings; as well as the negative aging effect with (1) the (SC, CB) coupling, (2) the (SC, VIS) coupling, and (3) the (SM, VIS) coupling. In comparison, the magnitude data analysis shows a different aging effect in the *mFCage* matrix in Fig. 4b.

Age effect on positive/negative couplings

We examine the structure of the age effect on resting-brain function connectivity in Figs. 5 and 6. Specifically, the magnitude data show that the significant positive couplings exhibit a deceasing trend with respect to brain age, which counters the increasing trend associated with the significant negative couplings (see Fig. 5a1, a2). On the contrary, the phase data show an increasing trend for significant positive couplings and a decreasing trend for significant negative couplings in Fig. 5b1, b2.

Furthermore, we observed the most significant positive coupling between two sensorimotor subfunctions (in SM domain) from magnitude data (in Fig. 6a1) and between subcortical subjections (in SC domain) from phase data (in Fig. 6b1); meanwhile, we also observed the most significant negative couplings from a (SM, DMN) coupling from magnitude data (in Fig. 6a2) and from a (SC, CB) coupling from phase data (in Fig. 6b2). As such, we have noted different subfunction coupling mechanisms behind the structure of brain age effect through magnitude and phase data. Nevertheless, both mechanisms embrace an antagonism (positive and negative cancelation) and converge to a balance in overall age effect. In particular, with phase data we observe that the most significant positive coupling in the resting-state brain dwell in the subcortical region (basal ganglia) and the most significant negative coupling occurs between the subcortical and cerebellum.

Understanding positive/negative couplings

Our experiment results show that magnitude and phase data produce positive and negative couplings in the whole-brain connectivity matrices. From the temporal correlation between two timecourses associated with two subfunctions, we understand a positive coupling resulting from two in-phase timecourses (either (−, −) or (+, +)) in pairwise combination or a negative coupling from two opposite timecourses (either (−, +) or (+, −)). In the linear mapping between the fieldmap and phase image, a phase signal may take on positive/negative values in reflecting the bipolar-valued field values per se. In biophysiology, a phase signal may take on excitatory/inhibitory response to a local functional activity; this is an additional factor for positive/negative coupling. In comparison, a magnitude signal only takes on nonnegative values. As such, a magnitude positive/negative coupling is only determined by the magnitude excitatory/inhibitory responses to the local function activities. Therefore, the phase connection sign is determined by various combinations among positive/negative signal expressions and excitatory/inhibitory responses, whereas the magnitude connection sign is by the combinations of magnitude excitatory/inhibitory responses. For example, we may observe a phase positive connection in pFC that is the correlation between two negative phase timecourses in a (−, −) combination, which may correspond to a magnitude negative connection in mFC as results from one inhibitory and one excitatory magnitude timecourse in a (−,+) combination. After all, the complete understanding of the positive/negative couplings in mFC and pFC requires the biophysiological BOLD information, which is beyond the experimental data analysis.

In summary, our magnitude fMRI data analysis shows the most significant age effect on the default mode network and sensorimotor network (see DMN: mICA42 in Fig. 6a2, SM: mICA9, mICA12 in Fig. 6a1) in resting state, which is basically agreeable with other researchers (Damoiseaux 2017; Ferreira et al. 2016; Wu et al. 2011). Nevertheless, our phase data analysis shows the most significant age effect on subcortical and cerebellum regions (see Fig. 6b1, b2). Although the magnitude and phase data reveal different age effects on the brain function connections (Figs. 5, 6), both data analyses conclude with a balanced whole-brain connectivity in resting-state across a lifespan [10, 76] years (Fig. 4a). As for this inconsistency, we cannot say whether magnitude or phase results are more correct, and rather we think it important to include the complementary information from both. Perhaps, the emergence of phase-informed brain functions may inspire neuroscientists to reexamine brain function connectivity previously only studied using fMRI magnitude data.

Based upon the results for magnitude and phase data, we can neither prove nor disprove which is the truth because of a lack of ground truth for in vivo brain function mapping. However, it is clear that both are providing structured and complementary information about brain functional connectivity.

Limitations and future research

This study has some limitations. First, we utilized the fMRI phase data for brain function analysis, which still suffers from suboptimal fMRI phase imaging in the state-of-the-art commercial Siemens scanners (Dagher and Nael 2017; Robinson et al. 2015, 2017a, b). Although a phase image represents a brain interior magnetic field map, it still suffers from a morphological distortion from the underlying brain magnetic source (specifically the brain tissue intrinsic magnetic susceptibility undergone magnetization in main field B_0) (Chen and Calhoun 2013). The correction of the morphological distortion (dipole effect) associated with the phase-based brain functional spatial maps requires the magnetic susceptibility source reconstruction (Chen and Calhoun 2013), an ongoing research topic.

Strictly speaking, age effects should be studied on the same subjects at different ages via a longitudinal study. In our study, we focus on cross-sectional age effects only, but hope to study longitudinal data in future work.

In this report, we only address the resting-state brain functions from healthy subjects. In future research, it will be interesting to observe aberrant brain function connectivity and age effect using a large number of data from disease-specific subjects based on both magnitude and phase data analyses, especially to observe the brain functional connectivity rebalance in the resting state of a diseased brain under deep brain stimulation treatment (Kringelbach et al. 2011). The same techniques can also be used to compare brain function in resting state and task performance.

Conclusion

A BOLD fMRI study produces a time series of magnitude and phase images in pairs, representing brain states in different measurements. Both magnitude and phase are equally useful for brain function study by providing complementary information from different perspectives. Based on 600-subject fMRI phase data analysis, we show that the human resting-brain function connectivity shows a positive/negative balance in whole-brain connectivity over an age span of [10, 76] years. By looking into the aging effect on significant positive and negative connections separately, we find that the positive connectivity increases slightly with age while the negative connectivity decreases slightly. In comparison, the magnitude data analysis offers different brain function depictions. In particular, our fMRI phase data analysis identified the most significantly coupled subfunctions in the subcortical and cerebellum regions in resting state, whereas the magnitude fMRI data analysis defined the pivot subfunctions in the default mode network and the sensorimotor region. Future research is needed to understand the different and complementary information captured from magnitude and phase data analysis.

Acknowledgements The authors would like to acknowledge the funding support of NIH Grant P20GM103472. The authors declare no competing financial interest.

Compliance with ethical standards

Conflict of interest The authors declare no conflict of interest.

Informed consent All the human subjects provided written consent for MRI scanning under the approval of IRB at the University of New Mexico.

References

Abou Elseoud A, Littow H, Remes J, Starck T, Nikkinen J, Nissila J, Timonen M, Tervonen O, Kiviniemi V (2011) Group-ICA model order highlights patterns of functional brain connectivity. Front Syst Neurosci 5:37

Adhikari MH, Hacker CD, Siegel JS, Griffa A, Hagmann P, Deco G, Corbetta M (2017) Decreased integration and information capacity in stroke measured by whole brain models of resting state activity. Brain 140(4):1068–1085

Allen EA, Erhardt EB, Damaraju E, Gruner W, Segall JM, Silva RF, Havlicek M, Rachakonda S, Fries J, Kalyanam R, Michael AM, Caprihan A, Turner JA, Eichele T, Adelsheim S, Bryan AD,

Bustillo J, Clark VP, Feldstein Ewing SW, Filbey F, Ford CC, Hutchison K, Jung RE, Kiehl KA, Kodituwakku P, Komesu YM, Mayer AR, Pearlson GD, Phillips JP, Sadek JR, Stevens M, Teuscher U, Thoma RJ, Calhoun VD (2011) A baseline for the multivariate comparison of resting-state networks. Front Syst Neurosci 5:2

Allen EA, Damaraju E, Plis SM, Erhardt EB, Eichele T, Calhoun VD (2014) Tracking whole-brain connectivity dynamics in the resting state. Cereb Cortex 24(3):663–676

Aragri A, Scarabino T, Seifritz E, Comani S, Cirillo S, Tedeschi G, Esposito F, Di Salle F (2006) How does spatial extent of fMRI datasets affect independent component analysis decomposition? Hum Brain Mapp 27(9):736–746

Arbabshirani MR, Calhoun VD (2011) Functional network connectivity during rest and task: comparison of healthy controls and schizophrenic patients. Conf Proc IEEE Eng Med Biol Soc 2011:4418–4421

Arja SK, Feng Z, Chen Z, Caprihan A, Kiehl KA, Adali T, Calhoun VD (2009) Changes in fMRI magnitude data and phase data observed in block-design and event-related tasks. Neuroimage 59(4):3748–3761

Balla DZ, Sanchez-Panchuelo RM, Wharton SJ, Hagberg GE, Scheffler K, Francis ST, Bowtell R (2014) Functional quantitative susceptibility mapping (fQSM). Neuroimage 100:112–124

Beckmann CF, DeLuca M, Devlin JT, Smith SM (2005) Investigations into resting-state connectivity using independent component analysis. Philos Trans R Soc Lond B Biol Sci 360(1457):1001–1013

Bianciardi M, van Gelderen P, Duyn JH (2014) Investigation of BOLD fMRI resonance frequency shifts and quantitative susceptibility changes at 7 T. Hum Brain Mapp 35(5):2191–2205

Bullmore E, Sporns O (2009) Complex brain networks: graph theoretical analysis of structural and functional systems. Nat Rev Neurosci 10(3):186–198

Calhoun VD, Adali T, Pearlson GD, Pekar JJ (2001) A method for making group inferences from functional MRI data using independent component analysis. Hum Brain Mapp 14(3):140–151

Calhoun VD, Liu J, Adali T (2009) A review of group ICA for fMRI data and ICA for joint inference of imaging, genetic, and ERP data. Neuroimage 45(1 Suppl):S163–S172

Caliandro P, Reale G, Vecchio F, Iacovelli C, Miraglia F, Masi G, Rossini PM (2017) Defining a functional network homeostasis after stroke: EEG-based approach is complementary to functional MRI. Brain 140(12):e71

Chen Z, Calhoun VD (2011) Two pitfalls of BOLD fMRI magnitude-based neuroimage analysis: non-negativity and edge effect. J Neurosci Methods 199(2):363–369

Chen Z, Calhoun V (2013) Understanding the morphological mismatch between magnetic susceptibility source and T2* image. Magn Reson Insights 6:65–81

Chen Z, Calhoun V (2015) Nonlinear magnitude and linear phase behaviors of T2* imaging: theoretical approximation and Monte Carlo simulation. Magn Reson Imaging 33(4):390–400

Chen Z, Calhoun V (2016) T2* phase imaging and processing for magnetic susceptibility mapping. Biomed Phys Eng Express 2:025015

Chen Z, Caprihan A, Damaraju E, Rachakonda S, Calhoun V (2018a) Functional brain connectivity in resting-state fMRI using phase and magnitude data. J Neurosci Methods 293:299–309

Chen Z, Robinson J, Calhoun V (2018b) Brain functional BOLD perturbation modelling for forward fMRI and inverse mapping. PLoS One 13(1):e0191266

Dagher J, Nael K (2017) MR phase imaging with bipolar acquisition. NMR Biomed 34(4):e3523

Damoiseaux JS (2017) Effects of aging on functional and structural brain connectivity. Neuroimage 160:32–40

Dodel S, Herrmann JM, Geisel T (2002) Functional connectivity by cross-correlation clustering. Neurocomputing 44–46:1065–1070

Du Y, Fan Y (2013) Group information guided ICA for fMRI data analysis. Neuroimage 69:157–197

Du Y, Pearlson GD, Liu J, Sui J, Yu Q, He H, Castro E, Calhoun VD (2015) A group ICA based framework for evaluating resting fMRI markers when disease categories are unclear: application to schizophrenia, bipolar, and schizoaffective disorders. Neuroimage 122:272–280

Erhardt EB, Rachakonda S, Bedrick EJ, Allen EA, Adali T, Calhoun VD (2011) Comparison of multi-subject ICA methods for analysis of fMRI data. Hum Brain Mapp 32(12):2075–2095

Feng Z, Caprihan A, Blagoev KB, Calhoun VD (2009) Biophysical modeling of phase changes in BOLD fMRI. Neuroimage 47(2):540–548

Ferreira LK, Regina AC, Kovacevic N, Martin Mda G, Santos PP, Carneiro Cde G, Kerr DS, Amaro E Jr, McIntosh AR, Busatto GF (2016) Aging effects on whole-brain functional connectivity in adults free of cognitive and psychiatric disorders. Cereb Cortex 26(9):3851–3865

Fox MD, Snyder AZ, Vincent JL, Corbetta M, Van Essen DC, Raichle ME (2005) The human brain is intrinsically organized into dynamic, anticorrelated functional networks. Proc Natl Acad Sci USA 102(27):9673–9678

Fox MD, Zhang D, Snyder AZ, Raichle ME (2009) The global signal and observed anticorrelated resting state brain networks. J Neurophysiol 101(6):3270–3283

Genovese CR, Lazar NA, Nichols T (2002) Thresholding of statistical maps in functional neuroimaging using the false discovery rate. Neuroimage 15(4):870–878

Guo Y, Pagnoni G (2008) A unified framework for group independent component analysis for multi-subject fMRI data. Neuroimage 42(3):1078–1093

Jafri MJ, Pearlson GD, Stevens M, Calhoun VD (2008) A method for functional network connectivity among spatially independent resting-state components in schizophrenia. Neuroimage 39(4):1666–1681

Kee Y, Liu Z, Zhou L, Dimov A, Cho J, de Rochefort L, Seo JK, Wang Y (2017) Quantitative susceptibility mapping (QSM) algorithms: mathematical rationale and computational implementations. IEEE Trans Biomed Eng 64(11):2531–2545

Kringelbach ML, Green AL, Aziz TZ (2011) Balancing the brain: resting state networks and deep brain stimulation. Front Integr Neurosci 5:8

Lewis LD, Setsompop K, Rosen BR, Polimeni JR (2016) Fast fMRI can detect oscillatory neural activity in humans. Proc Natl Acad Sci USA 113(43):E6679–E6685

Li YO, Adali T, Calhoun VD (2007) A feature-selective independent component analysis method for functional MRI. Int J Biomed Imaging 2007:15635

Litwin-Kumar A, Doiron B (2012) Slow dynamics and high variability in balanced cortical networks with clustered connections. Nat Neurosci 15(11):1498–1505

Liu Y, Huang L, Li M, Zhou Z, Hu D (2015) Anticorrelated networks in resting-state fMRI-BOLD data. Bio Med Mater Eng 26(Suppl 1):S1201–S1211

Marino J, Schummers J, Lyon DC, Schwabe L, Beck O, Wiesing P, Obermayer K, Sur M (2005) Invariant computations in local cortical networks with balanced excitation and inhibition. Nat Neurosci 8(2):194–201

McKeown MJ, Sejnowski TJ (1998) Independent component analysis of fMRI data: examining the assumptions. Hum Brain Mapp 6(5–6):368–372

McKeown MJ, Hansen LK, Sejnowsk TJ (2003) Independent component analysis of functional MRI: what is signal and what is noise? Curr Opin Neurobiol 13(5):620–629

Meadows R (2011) Finding balance in cortical networks. PLoS Biol 9(3):e1001035

Menon RS (2002) Postacquisition suppression of large-vessel BOLD signals in high-resolution fMRI. Magn Reson Med 47(1):1–9

Murphy K, Birn RM, Handwerker DA, Jones TB, Bandettini PA (2009) The impact of global signal regression on resting state correlations: are anti-correlated networks introduced? Neuroimage 44(3):893–905

Ozbay PS, Warnock G, Rossi C, Kuhn F, Akin B, Pruessmann KP, Nanz D (2016) Probing neuronal activation by functional quantitative susceptibility mapping under a visual paradigm: a group level comparison with BOLD fMRI and PET. Neuroimage 137:52–60

Robinson SD, Dymerska B, Bogner W, Barth M, Zaric O, Goluch S, Grabner G, Deligianni X, Bieri O, Trattnig S (2015) Combining phase images from array coils using a short echo time reference scan (COMPOSER). Magn Reson Med 77:318–327

Robinson SD, Bredies K, Khabipova D, Dymerska B, Marques JP, Schweser F (2017a) An illustrated comparison of processing methods for MR phase imaging and QSM: combining array coil signals and phase unwrapping. NMR Biomed 30(4):e3601

Robinson SD, Dymerska B, Bogner W, Barth M, Zaric O, Goluch S, Grabner G, Deligianni X, Bieri O, Trattnig S (2017b) Combining phase images from array coils using a short echo time reference scan (COMPOSER). Magn Reson Med 77(1):318–327

Rowe DB (2005) Modeling both the magnitude and phase of complex-valued fMRI data. Neuroimage 25(4):1310–1324

Rowe DB (2009) Magnitude and phase signal detection in complex-valued fMRI data. Magn Reson Med 62(5):1356–1357 **(author reply 1358-60)**

Rubinov M, Sporns O (2010) Complex network measures of brain connectivity: uses and interpretations. Neuroimage 52(3):1059–1069

Schweser F, Deistung A, Reichenbach J (2016) Foundations of MRI phase imaging and processing for quantitative susceptibility mapping (QSM). Z Med Phys 26(1):6–34

Wu JT, Wu HZ, Yan CG, Chen WX, Zhang HY, He Y, Yang HS (2011) Aging-related changes in the default mode network and its anti-correlated networks: a resting-state fMRI study. Neurosci Lett 504(1):62–67

Xu J, Potenza MN, Calhoun VD (2013) Spatial ICA reveals functional activity hidden from traditional fMRI GLM-based analyses. Front Neurosci 7:154